Directional Acoustic Superscattering by Coupled Resonators

Taehwa Lee ,[*] Tsuyoshi Nomura, Paul Schmalenberg, Ercan M. Dede, and Hideo Iizuka
Toyota Research Institute of North America, Toyota Motor North America, Ann Arbor, Michigan 48105, USA

We demonstrate acoustic superscattering from a subwavelength scatterer consisting of multiple deep-subwavelength resonators. We show that superscattering is enabled by strong coupling between these resonators and the discrete rotational symmetry of the scatterer results in angle-dependent superscattering. From the cylindrical-wave expansion of an incident plane wave, we observe that radially arranged resonators can effectively couple to these expanded cylindrical waves. In addition, we provide an analytical model characterizing the coupled resonators, providing a critical understanding of superscattering. As an experimental demonstration, we present a superscatterer with six acoustic resonators that shows angle-dependent superscattering.

I. INTRODUCTION

Wave scattering from objects is a fundamental phenomenon regarding wave-matter interactions [1,2]. Scattering from a subwavelength structure occurs via angular momentum channels; each single channel has a scattering cross-section limit (σ_0) of $2\lambda/\pi$ in two dimensions [3] or $3\lambda^2/2\pi$ in three dimensions [4]. Control of wave scattering is shown in two extreme cases: cloaking (scattering cancellation) [5,6] and superscattering [3,4,7–9]. In particular, superscattering that demonstrates a scattering cross section far greater than that of the single channel limit (e.g., $> 3\sigma_0$) is of fundamental importance, enabling a rich variety of intriguing physics and practical applications (e.g., sensing, energy harvesting) [10–14]. In theory, an arbitrary large scattering cross section (i.e., superscattering) is enabled by the orthogonality of these channels, when a sufficient number of channels are excited for degenerate resonances. The concept of superscattering has been theoretically demonstrated in electromagnetic waves using a core-shell multilayer structure [3,4,7], and, more recently, it has been experimentally realized in the microwave regime [8], thus making it possible to explore new applications.

Similar to electromagnetic superscattering, acoustic superscattering can provide new possibilities by maximizing the interaction of an acoustic wave with structures (e.g., acoustic sensing [15] and energy harvesting [16]). There have been many studies investigating acoustic scattering [17–20]; however, scattering phenomena are far different from superscattering of subwavelength scatterers that require multiple excited channels at a single frequency. For example, acoustic Mie scatterers have shown multiple-mode excitations (monopole, dipole, and quadrupole), but each mode at a different frequency [21]. In addition, core-shell multilayered optical superscatterers cannot be directly extended to an acoustic superscatterer because of limited materials with a target refractive index. Therefore, it is challenging to demonstrate acoustic superscattering. Although superscattering has been thoroughly studied in terms of angular momentum channels [3,4], there are still theoretical questions requiring further investigation. For instance, what is the theoretical limit of the highest number of angular momentum channels (>4), and why do higher angular momentum channels have relatively narrower frequency bandwidths? Another interesting question is whether scatterers composed of multiple resonators can excite a sufficient number of angular momentum channels for superscattering. In such a case, the constituent resonators strongly couple with each other [9,22], and thus, the orthogonality of resonances is not guaranteed. Moreover, new features, such as angle-dependent superscattering, can be useful for directional sensing [23,24] and scattering pattern shaping [25,26], while maintaining superior scattering performance.

We experimentally and theoretically demonstrate acoustic superscattering from a subwavelength structure. The structure consists of a subwavelength cylindrical scatterer decorated with multiple acoustic resonators that enable effective coupling of the resonators with angular momentum channels. We find that the scatterers show angle-dependent superscattering. In addition, our analytical model captures coupling between resonators to provide a critical understanding of superscattering. Lastly, we experimentally show superscattering from a solid cylinder composed of six Helmholtz resonators by considering acoustic intrinsic losses.

————————
[*]taehwa.lee@toyota.com

II. RESULTS AND DISCUSSION

A. Superscattering by coupled resonators

Strong scattering from a subwavelength structure requires strong coupling between the incident wave and structure. To gain an insight into such a coupling phenomenon, we start by considering incident plane waves of wave vector $\mathbf{k}_w = (k_w\cos\psi_0, k_w\sin\psi_0)$, where ψ_0 is the angle of incidence, which can be expressed by the Jacobi expansion [27],

$$p_{\text{int}}(\mathbf{r}) = p_0 e^{i\mathbf{k}_w \cdot \mathbf{r}} = p_0 \sum_{n=-\infty}^{\infty} e^{in(\pi/2+\theta-\psi_0)} J_n(k_w r), \quad (1)$$

where (r, θ) are the polar coordinates and J_n is the nth-order Bessel function of the first kind. Equation (1) indicates that the incident plane wave can be decomposed into cylindrical waves, each of which is denoted as a momentum channel, n. To effectively couple these cylindrical wave channels, we conceive a subwavelength scatterer with radially arranged resonators, as illustrated in Fig. 1(a). Here, the six resonators ($N = 6$) are either identical (type II) or partially detuned (type I). As shown in Fig. 1(a),

superscattering by the radially arranged resonators significantly perturbs the incident plane wave, thus casting a shadow on the total pressure field (bottom) and exhibiting strong downstream scattering in the scattering pattern (top). These characteristics are in a sharp contrast to scattering by a rigid cylinder of the same radius [Fig. 1(b)].

Figure 1(c) shows the scattering cross section of the cylinder scatterer (diameter $2R = 100$ mm) with the detuned lossless resonators (type I). Here, the resonance frequencies of the detuned resonators $j = 1$ and 4 (orange rectangles in type I) are blueshifted by approximately 300 Hz, leading to a vibration phase shift of approximately $\pi/2$. Remarkably, the lossless scatterer with detuned resonators shows a total scattering cross section of 6.3 times that of the single-channel limit ($2\lambda/\pi$) at 1870 Hz ($\lambda = 183$ mm; $2R/\lambda = 0.55$), which is larger than 5.2 for the same size scatterer, but with six identical resonators (type II; see note 1 within the Supplemental Material [28]). We find that the enhancement occurs because detuning of the $j = 1$ and 4 resonators improves the contribution of the $|n| = 1$ momentum channel at 1870 Hz by redshifting the spectrum of $|n| = 1$. The analytical results (red solid line) obtained from Eq. (8) show excellent agreement with the
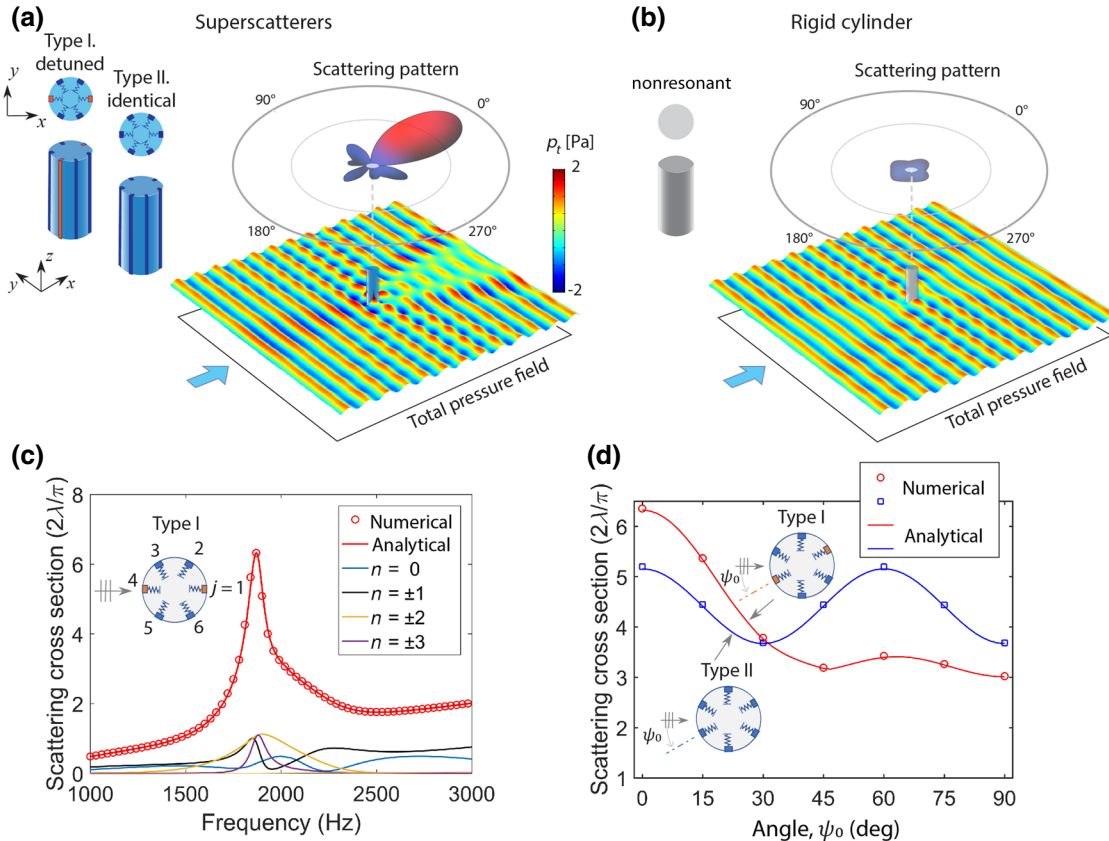

FIG. 1.   Superscattering of a cylinder with $N = 6$ resonators. (a) Superscattering by coupled resonators, showing scattering pattern (top) and total pressure field (bottom). (b) Scattering by a rigid cylinder. (c) Superscattering of a scatterer with harmonic oscillator $N = 6$. The symbols indicate the COMSOL results, while the solid lines indicate the analytical results. (d) Angle-dependent superscattering for scatterers with detuned resonators (red circles and line) and identical resonators (blue squares and line).

numerical results (red symbols). Despite the discrete radial arrangement, the degeneracy of the nth and $-n$th angular momentum channels is confirmed [i.e., scattering cross section $C_{sct,n} = C_{sct,-n}$ and $C_{sct,n} + C_{sct,-n} = 2(2\lambda/\pi)$]. Notably, the theoretical scattering cross-section limit of $7(2\lambda/\pi)$ for the $N = 6$ scatterer cannot be reached because a negligible contribution of the $n = 0$ channel occurs due to cancellation of the resonant scattering by direct scattering (see note 2 within the Supplemental Material [28]).

Due to their discrete radial symmetry [29], the superscatterers enable angle-dependent superscattering, as shown in Fig. 1(d). Here, the incident angle, ψ_0, of the plane wave affects coupling between the constituent resonators via the angle-dependent excitation phases, ϕ_j [i.e., $\phi_j - \phi_1 = (2\pi/\lambda)D \sin(\theta_j/2) \sin(\theta_j/2 - \psi_0)$], and the force term, f, in Eq. (8). Notably, the superscatterer with detuned resonators (C_2 symmetry) exhibits a significant difference of C_{sct} between $\psi_0 = 0$ and $\psi_0 \geq 30°$, while the scatterer with identical resonators (C_6 symmetry) shows an expected angularly periodic behavior with ψ_0.

B. Acoustic coupled mode theory for coupled resonators

To investigate the scattering from a scatterer composed of multiple resonators, we develop a full analytical model based on coupling between the resonators. To generalize

our analysis, regardless of the resonator types, we use a harmonic oscillator (HOS) model. For resonators much smaller than the cylinder, the scattered pressure [$p_{sct}(\mathbf{r})$] is modeled by the direct (p_{dir}) and resonant (p_{res}) scatterings as [30]

$$p_{sct}(\mathbf{r}) = p_{dir}(\mathbf{r}) + p_{res}(\mathbf{r}). \qquad (2)$$

Here, the direct scattering corresponds to a contribution from the same size cylinder without resonators [31],

$$p_{dir}(\mathbf{r}) = -p_0 \sum_{n=-\infty}^{\infty} i^n \frac{J'_n(k_w R)}{H'_n(k_w R)} H_n(k_w r)e^{in\theta}, \qquad (3)$$

where H_n is the nth-order Hankel function of the first kind. The resonant scattering is determined by the pressure generated by a resonator with uniform velocity, v_j, on the surface of a cylinder with radius, R [32,33],

$$p_{res}(\mathbf{r}) = \sum_{j=1}^{N} p_{res,j}, \qquad (4a)$$

$$p_{res,j}(\mathbf{r}) = -\frac{i\omega\rho}{4\pi} \int_0^{2\pi} v_j \, G(r, R, \theta, \theta_j)d\theta_j, \qquad (4b)$$

where $G(r, R, \theta, \theta_i) = -(2/k_w R) \sum_{n=-\infty}^{\infty}[H_n(k_w r)/H'_n(k_w R)]e^{in(\theta-\theta_j)}$ is the Green's function chosen for

(a) $n = 0$ $n = 1$ $n = 2$ $n = 3$ $n = 4$

$r_p = 0.29\lambda$ $r_p = 0.49\lambda$ $r_p = 0.7\lambda$ $r_p = 0.89\lambda$

(b) Resonator $N = 1$ $N = 2$ $N = 4$ $N = 6$ $N = 8$

(c) $N = 1$, $n = 0$ $N = 2$, $n = \pm1$ $N = 4$, $n = \pm2$ $N = 6$, $n = \pm3$ $N = 8$, $n = \pm4$

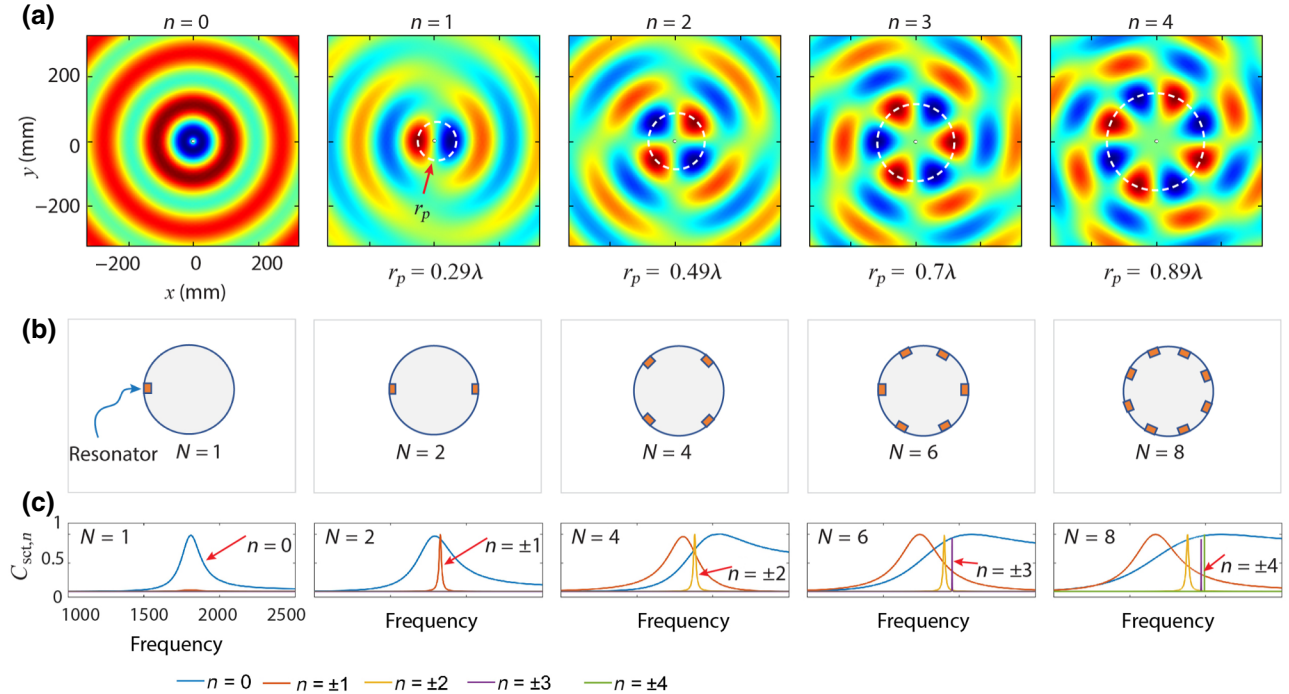— $n = 0$ — $n = \pm1$ — $n = \pm2$ — $n = \pm3$ — $n = \pm4$

FIG. 2. Superscattering by multiple resonators for excitation of incident channels. (a) Expansion of incident plane waves for channels ($n = 0, 1, 2, 3, 4$). Decomposed pressure fields (real parts) of each channel. The dashed white circles, with a radius of r_p, indicate the first peak amplitudes with respect to r. (b) Schematics of cylindrical scatterers consisting of N number of resonators. The resonators N are radially arranged for channel $n = N/2$. (c) Scattering cross section (normalized by $2\lambda/\pi$) of each angular momentum channel for N number of resonators (diameter $D = 10$ mm for $N = 1$ and 2; and $D = 40$ mm for $N = 4, 6$, and 8) obtained by using Eq. (9).
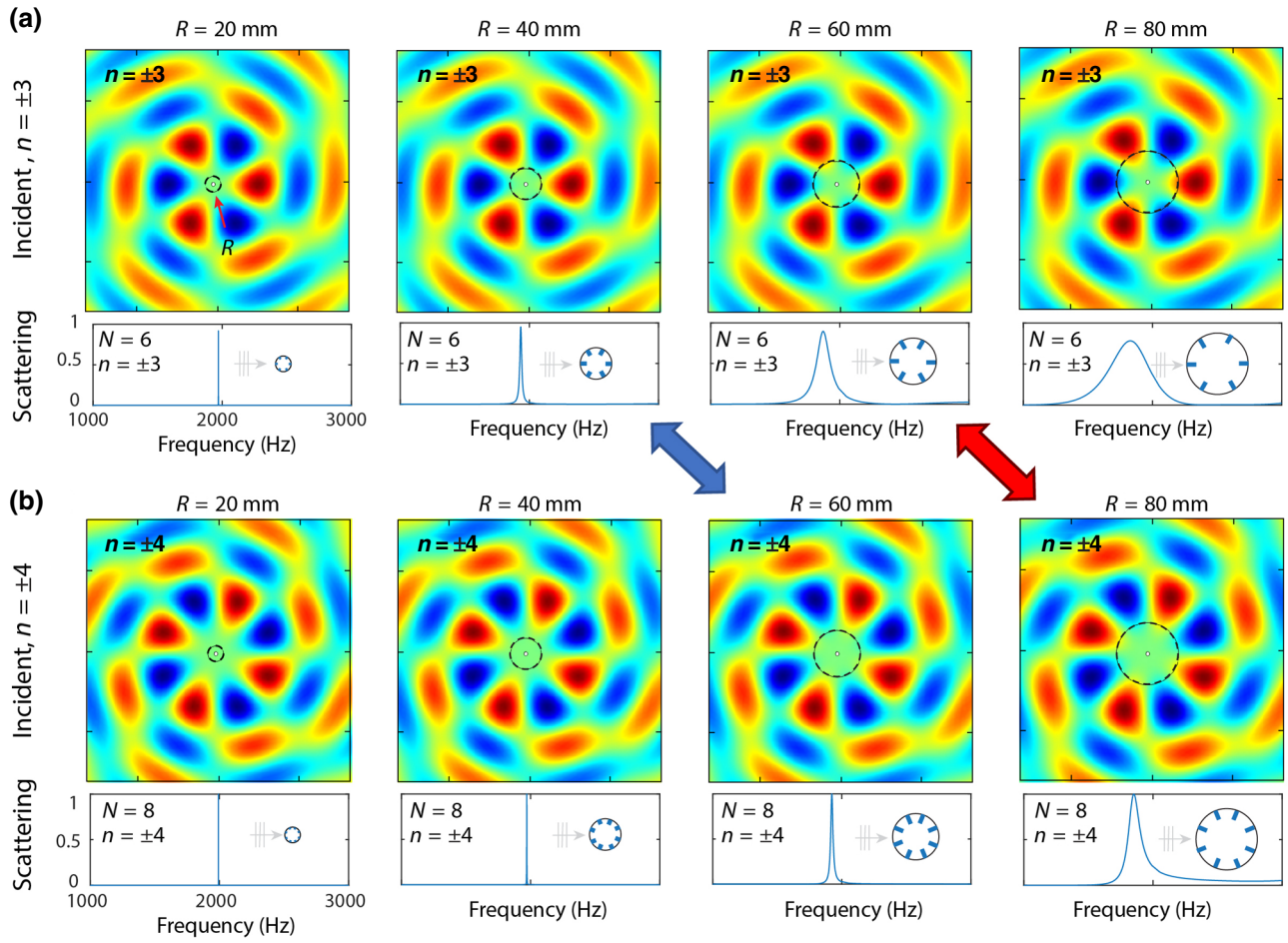
FIG. 3. Frequency bandwidth of scattering channels with respect to the size of scatterers. (a) Incident pressure field of $n = \pm3$ overlaid with dashed circles of radii R. Contribution of scattering channel $n = \pm3$ for scatterers of $N = 6$ and different radii ($R = 20, 40, 60$ and 80 mm). (b) Incident pressure field of $n = \pm4$. Contribution of scattering channel $n = \pm4$ for scatterers of $N = 8$. The blue and red arrows indicate the cases showing similar frequency bandwidths.

$\partial G/\partial r = 0$ on the cylinder surface. Notably, the resonant scattering depends on the velocity of the coupled resonators. The response of each resonator can be calculated by the coupled equation of motion [34]:

$$(-\omega^2 \mathbf{M} - i\omega \mathbf{C} + \mathbf{K})\mathbf{x} = \mathbf{f}, \qquad (5)$$

where $\mathbf{M}$ is the diagonal matrix of mass given by $\mathrm{diag}(m_1, m_2, \ldots, m_N)$, and $\mathbf{K}$ is the diagonal matrix of stiffness, $\mathrm{diag}(k_1, k_2, \ldots, k_N)$. The damping matrix, $\mathbf{C}$, is given by

$$\mathbf{C} = \begin{bmatrix} c_{11} + \delta_1 & c_{12} & c_{13} & \cdots & c_{1N} \\ c_{21} & c_{22} + \delta_2 & c_{23} & \cdots & c_{2N} \\ c_{31} & c_{32} & c_{33} + \delta_3 & \cdots & c_{3N} \\ \vdots & \vdots & \vdots & \ddots & \vdots \\ c_{N1} & c_{N2} & c_{N3} & \cdots & c_{NN} + \delta_N \end{bmatrix}. \qquad (6)$$

Here, the diagonal elements of $\mathbf{C}$ describe radiation leakage (c_{ii}) and intrinsic loss (δ_i), and the off-diagonal elements (c_{ij} for $i \neq j$) describe coupling between the resonators [22]. By using Eq. (4b), both radiation leakage ($i = j$) and coupling rate ($i \neq j$) are analytically determined by [35,36]

$$c_{ij} = \frac{\int_{S_i} p_{\mathrm{res},j}(\vec{r})dS}{v_j} = \frac{i\omega\rho s}{2\pi k_w R} \sum_{n=-\infty}^{\infty} \frac{H_n(k_w R)}{H'_n(k_w R)} e^{in(\theta_i - \theta_j)}. \qquad (7)$$

Here, the leakage rate of each channel ($c_{ii,n}$) determines coupling of the constituent resonators with scattered waves of the channel, and thus, its frequency bandwidth. The elements of the force matrix, f, are determined with the total pressure field for the nonresonant scatterer [i.e., $p_{\mathrm{tot}} = p_{\mathrm{int}}(\mathbf{r}) + p_{\mathrm{dir}}(\mathbf{r})$]. By integrating p_{tot} over the resonator j (area of S_j), the force acting on resonator j is

expressed by

$$f_j = \int_{S_j} [p_{\text{int}}(\mathbf{r}) + p_{\text{dir}}(\mathbf{r})] dS. \quad (8)$$

From Mie scattering theory, the scattering cross section is given by $C_{\text{sct}} = \sum_{n=-\infty}^{\infty} (2\lambda/\pi)|S_n|^2$, where S_n is the scattering coefficient [37]. With Eqs. (3) and (4), we derive the scattering coefficient,

$$|S_n| = |S_{\text{dir},n} + S_{\text{res},n}|$$
$$= \left| \frac{J'_n(k_w R)}{H'_n(k_w R)} + \frac{i^{1-n}\omega\rho}{2\pi k_w R} \sum_{j=1}^{N} \frac{s_j v_j}{H'_n(k_w R)} e^{in(\psi_0-\theta_j)} \right|. \quad (9)$$

Here, $|S_{\text{dir},n}|^2 \le 1$ and $|S_{\text{res},n}|^2 \le 1$ leads to $|S_n|^2 \le 2$, i.e., $C_{\text{sct},n} \le (4\lambda/\pi)$.

C. Highest $|n|$ and bandwidth of the scattering channels

To further gain an insight into scattering channels and understand why we choose a specific number of resonators (i.e., $N = 6$) for superscattering, we pay attention to the decomposed cylindrical waves from Eq. (1), which are shown in Fig. 2(a). From these incident pressure fields, we postulate that these incident channels, n, can effectively couple to N number of resonators on a scatterer, if these resonators are radially arranged near the high-amplitude regions of the pressure fields (i.e., $|n| = N/2$, where N is an even number), as illustrated in Fig. 2(b). Indeed, we find that these radially arranged resonators can excite scattering channels of $|n| \le N/2$, as the contribution of each

scattering channel is shown in Fig. 2(c). Notably, there is no theoretical limit, as long as a sufficient number of resonators are radially arranged (e.g., $|n| \ge 5$ for $N \ge 10$); see note 3 within the Supplemental Material [28].

Practically, the number of resonators is constrained because the highest $|n|$ exhibits a relatively narrow bandwidth of the scattering channels [see $n = \pm 4$ and $N = 8$ in Fig. 2(c)]. We observe that the frequency bandwidth critically depends on the size of a scatterer, relative to the high-amplitude region (a radius of r_p) of each incident channel [see white dashed circles in Fig. 2(a)]. Figure 3 shows incident pressure fields overlaid with scatterers of different radii (dashed circles). With increasing R, the overlap between the scatterers and high-amplitude regions is enhanced, resulting in increased bandwidths. For the same radius, owing to its smaller r_p, the overlap of $n = \pm 3$ [shown in Fig. 3(a)] is clearer than that of $n = \pm 4$ in Fig. 3(b), thus producing better coupling, and thereby, larger bandwidths. The bandwidth of $n = \pm 3$ for a specific radius, R, is similar to that of $n = \pm 4$ for a larger radius. Specifically, $n = \pm 4$ for $R = 60$ mm has a similar bandwidth to that of $n = \pm 3$ for $R = 40$ mm (see blue arrow), while $n = \pm 4$ for $R = 80$ mm corresponds to $n = \pm 3$ for $R = 60$ mm (see red arrow). In addition, the superscatterer of $N = 8$ requires a relatively large size for the sizable bandwidths and degenerate resonances (see note 4 within the Supplemental Material [28]).

D. Angle-dependent superscattering owing to discrete radial symmetry

The incident-angle dependence is caused by the alignment of resonators with respect to the incident cylindrical waves; the incident fields of $n = \pm 3$ are shown
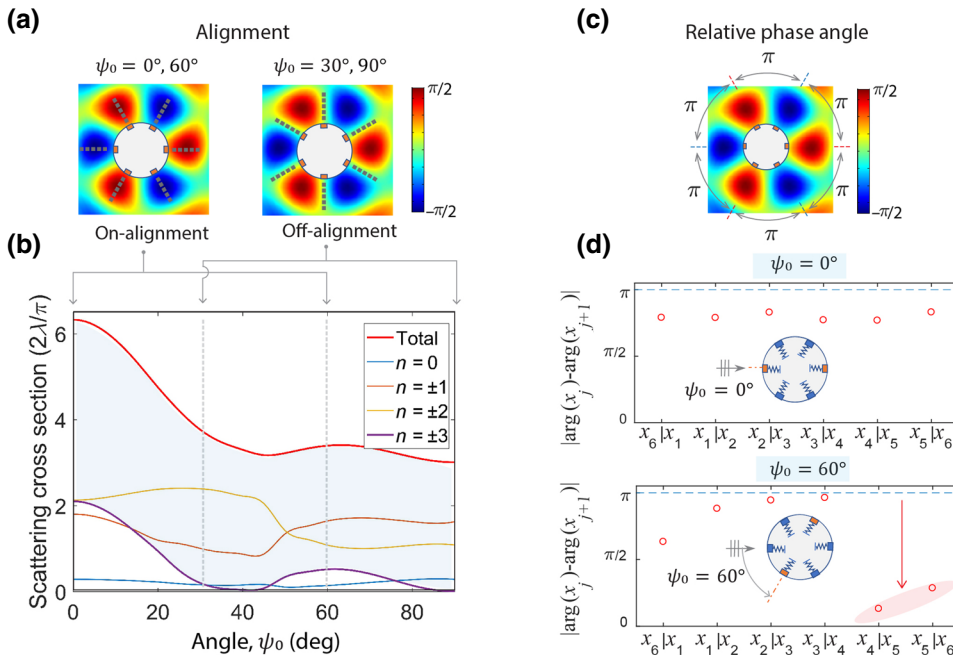

FIG. 4. Incident-angle-dependent acoustic superscattering. (a) Alignment of the resonators with respect to the incident pressure field of $n = \pm 3$, exhibiting on alignment for $\psi_0 = 0°$ and $60°$ and off alignment for $\psi_0 = 30°$ and $90°$. The dashed lines guide the alignment of the resonators with respect to the pressure fields. (b) Incident-angle-dependent contribution of each scattering channel. The blue shade assists in identifying similarity between $n = \pm 3$ and total scattering. (c) Incident pressure field of $n = \pm 3$, showing a phase angle difference of π between the neighboring high-amplitude regions. (d) Vibration phase difference between neighboring resonators i and j (i.e., $x_i|x_j$) for $\psi_0 = 0°$ and $60°$.
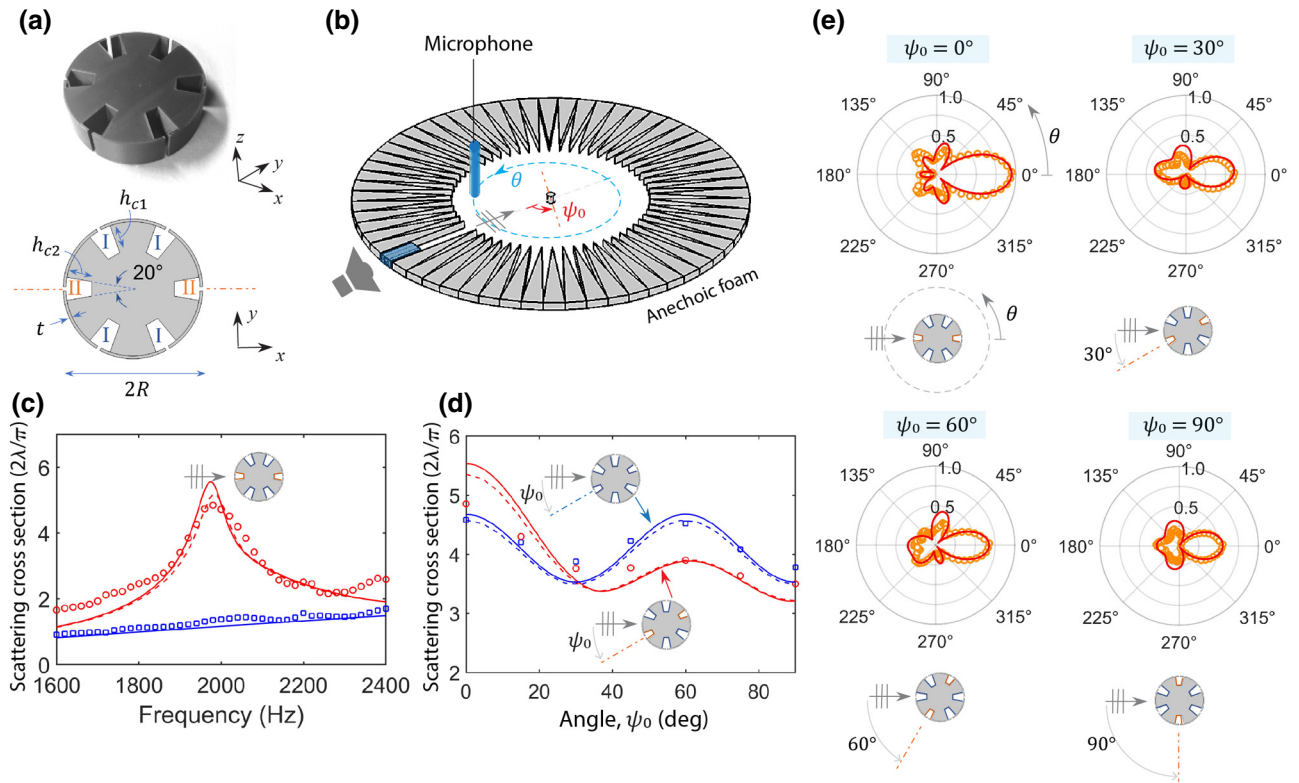
FIG. 5.   Measurement of acoustic superscattering. (a) Photograph of a 3D-printed device (25 mm height) and schematic of a super-scatterer with six Helmholtz resonators (two types of cavities: I and II). (b) Measurement setup for scattering cross section and radiation pattern. (c) Measured scattering cross section of the superscatterer for $\psi_0 = 0°$. The symbols indicate the measurement results, while the solid (dashed) lines indicate the numerical (analytical) results. For comparison, a solid cylinder of the same size is plotted as the blue line and symbols. (d) Peak scattering cross section of superscatterers with the detuned Helmholtz resonators (red) and identical Helmholtz resonators (blue) as a function of the incident angles, ψ_0. The symbols indicate the measurement results, while the solid (dashed) lines indicate the numerical (analytical) results. (e) Scattered radiation patterns from the superscatterer with the detuned resonators for $\psi_0 = 0°$, $30°$, $60°$, and $90°$. The numerical results (solid lines) are overlaid with the measured results (symbols).

in Fig. 4(a). When the resonators are aligned to the high-amplitude regions of the pressure field, coupling between the resonators and pressure field occurs. The detuned resonators play a critical role in angle dependence (see note 5 within the Supplemental Material [28]). In Fig. 4(b), we observe that the contribution of the highest channel determines the overall angle dependence, as the trend of the total scattering cross section is very similar to that of $|n| = 3$. In particular, for $\psi_0 = 30°$, the contribution of the $|n| = 3$ momentum channel is negligible because of the off alignment of the resonators to the pressure $|n| = 3$ field and consequently undercoupling. For $\psi_0 = 60°$, the alignment is in favor of efficient coupling, yet the scattering is relatively low. In addition to the alignment, we find one more requirement regarding the vibrational phase of the resonators; the vibrational phase difference between adjacent resonators $[|\arg(x_j) - \arg(x_{j+1})|]$ should be π for excitation of $|n| = 3$ channels, as shown in Fig. 4(c). Notably, the detuned resonators show a deviation from π for $\psi_0 = 60°$. For oblique incident angles, $\psi_0 \neq 0, 90°$,

the C_2 symmetry scatterer shows lifted degeneracy of the nth and $-n$th angular momentum channels, i.e., $C_{\mathrm{sct},n} \neq C_{\mathrm{sct},-n}$.

E. Experimental demonstration of superscattering

We experimentally demonstrate superscattering, considering realistic acoustic losses. Our theoretical analysis, based on a HOS model, can be applied to any type of acoustic resonator [38–40] for superscattering. Here, we choose Helmholtz resonators and fabricate a cylindrical scatterer ($2R = 100$ mm) consisting of six Helmholtz resonators (HRs) using a 3D printer, as shown in Fig. 5(a). To measure the total scattering cross section, the device (25 mm height) is placed at the center of a two-dimensional waveguide ($r = 0$), as illustrated in Fig. 5(b). The total scattering cross section is calculated by $C_{\mathrm{sct}} = \int_0^{2\pi} |p_{\mathrm{sct}}(r_d, \theta)|^2 r_d d\theta / |p_{\mathrm{inc}}(r = 0)|^2$, where r_d is the detector's radius-of-rotation. The scattered pressure $[p_{\mathrm{sct}}(r_{\mathrm{d}}, \theta)]$ is calculated from measured p_{tot} and p_{inc}, i.e., $p_{\mathrm{sct}}(r_{\mathrm{d}}, \theta) =$

$p_{tot}(r_d) - p_{inc}(r_d)$. Here, p_{tot} and p_{inc} are measured at $r_d = 250$ mm (1.5λ) with and without the superscatterer, respectively.

Figure 5(c) shows the measured scattering cross section (symbols) for $\psi_0 = 0°$. The measured scattering cross section is approximately five times the single-channel limit at 1980 Hz, thus demonstrating superscattering, despite thermoviscous losses. For comparison, a rigid cylinder $(R = 50$ mm) without resonators shows only 1.5 times enhancement at the same frequency. The numerical (solid line) and analytical (dashed line) results capture the trends of the measurement results (symbols). The analytical results are obtained by using Eq. (9) with effective parameters that take into account Helmholtz resonators [41,42] (see note 6 within the Supplemental Material [28]). The discrepancy between the simulation and measurement is likely to be attributable to underestimated material-related losses in the HRs and imperfection of the anechoic foam. We experimentally confirm angle-dependent superscattering by the scatterer of $N = 6$, as shown in Fig. 5(d). The measurement results (symbols) shown are in broad agreement with the numerical (solid line) and analytical (dashed line) results, thus supporting the conclusion that the scatterer with detuned HRs is more effective in angular response than the scatterer with identical HRs. In addition, Fig. 5(e) shows the measured scattered pressure patterns $[|p_{sct}(r_d, \theta)|]$ from the superscatterer with the detuned HRs. The measurement results (symbols) are consistent with the numerical results (solid line). Regardless of the incident angles, ψ_0, the maximum scattered pressure amplitude is observed at $\theta = 0°$. For oblique angles, $\psi_0 \neq 0°$, scattering in other angles $\theta \neq 0°$ becomes considerable. For example, $\psi_0 = 30°$ leads to dominant scattering and the angles $\theta = 0°$, $90°$, and $180°$. This result demonstrates that the superscatterer based on coupled resonators enables effective control of the scattering radiation pattern.

III. CONCLUSION

We demonstrate acoustic superscattering in two dimensions from a subwavelength cylinder decorated with smaller scale resonators. Our work, based on coupled resonators, provides a promising approach to directional superscattering and provides a critical understanding of angular momentum channels for superscattering. Our work can offer alternative possibilities for ultrasparse noise barriers [21] and angle-dependent superscattering for directional acoustic wave control [17,43]. In addition, the acoustic superscatterer design can be extended to three dimensions and involve other types of acoustic resonators (e.g., membrane-type resonators [40] and quarter-wavelength resonators [39,44]). The concept is further applicable to subwavelength optical scatterers comprising deep-subwavelength resonant particles [45,46].

APPENDIX A: NUMERICAL SIMULATION

The numerical simulation is performed using a commercial finite-element-method solver, COMSOL v5.3. In the simulations using a harmonic oscillator model, the spring-mass system is modeled as a rigid rectangular mass subject to a spring boundary and acoustic-structure interaction boundary. All resonators have the same mass $(m_j = m_0 = 1.3 \times 10^{-6}$ kg), and each resonator width $(s_j = s_0 = 1$ mm) is much smaller than that of the diameter $2R = 100$ mm. For the detuned resonators, their stiffnesses are numerically optimized, with stiffnesses of $k_{2,3,5,6} = k_0 = 462$ N/m and $k_{1,4} = 1.2k_0$ (see note 7 within the Supplemental Material [28]). For COMSOL simulations using HRs, the simulations account for thermoviscous losses in HRs.

APPENDIX B: MEASUREMENT OF SCATTERING CROSS SECTION

Each HR is composed of a slit and cavity. The slit sizes of the HRs are the same $(w_n = 3$ mm and $t = 2$ mm). For detuning of the two HRs, smaller cavity sizes are used $(h_{c1} = 20.5$ mm, $h_{c2} = 18$ mm). The scattering cross section and scattering radiation pattern are characterized by the spinning microphone setup (see Fig. S10 within the Supplemental Material [28]), consisting of two acrylic sheets ($1/2''$ thick, $48'' \times 48''$), a full-range speaker ($2\frac{1}{2}''$, model SB65WVAC25-4, SB Acoustics, http://www.sbacoustics.com/) with a square waveguide ($20 \times 20 \times 150$ mm³), a motorized rotation stage (PRMTZ8, Thorlabs, New Jersey, USA), a pressure-field microphone and preamplifier ($1/4''$ prepolarized, sensitivity 1 mV/Pa, model 378C10, PCB Piezotronics, NY, USA), an audio power amplifier (model APA150, Daytonaudio), a data acquisition device (24-bit, 102.4 kS/s, model NI USB-4431, National Instruments), and anechoic termination (polyurethane foam). To record acoustic signals, the two microphones (1 and 2), connected to the two rotating arms of the rotation stage through magnet pairs, measure acoustic signals at an interval of $\Delta\theta = 5°$ for $\theta = 0°-360°$. Microphone 3 measures the incident pressure at the center $(r = 0)$. For characterization of angle-dependent superscattering, the scatterers are manually rotated for $\psi_0 = 0°-90°$ $(\Delta\psi_0 = 15°)$. The validation of the measurement setup is given in note 8 within the Supplemental Material [28].

[1] L. Rayleigh, On the scattering of light by small particles, Philos. Mag. **41**, 447 (1871).

[2] C. F. Bohren and D. R. Huffman, *Absorption and Scattering of Light by Small Particles* (Wiley, New York, 1983).

[3] Z. Ruan and S. Fan, Superscattering of Light from Subwavelength Nanostructures, Phys. Rev. Lett. **105**, 013901 (2010).

[4] Z. Ruan and S. Fan, Design of subwavelength super-scattering nanospheres, Appl. Phys. Lett. **98,** 043101 (2011).

[5] D. Schurig, J. J. Mock, B. J. Justice, S. A. Cummer, J. B. Pendry, A. F. Starr, and D. R. Smith, Metamaterial electromagnetic cloak at microwave frequencies, Science **314,** 977 (2006).

[6] Andrea Alù and Nader Engheta, Multifrequency Optical Invisibility Cloak with Layered Plasmonic Shells, Phys. Rev. Lett. **100,** 113901 (2008).

[7] C. Qian, X. Lin, Y. Yang, X. Xiong, H. Wang, E. Li, I. Kaminer, B. Zhang, and H. Chen, Multifrequency super-scattering from subwavelength hyperbolic structure, ACS Photonics **5,** 1506 (2018).

[8] C. Qian, X. Lin, Y. Yang, X. Xiong, H. Wang, E. Li, I. Kaminer, B. Zhang, and H. Chen, Experimental Observation of Superscattering, Phys. Rev. Lett. **122,** 063901 (2019).

[9] L. Verslegers, Z. Yu, Z. Ruan, P. B. Catrysse, and S. Fan, From Electromagnetically Induced Transparency to Superscattering with a Single Structure: A Coupled-Mode Theory for Doubly Resonant Structures, Phys. Rev. Lett. **108,** 083902 (2012).

[10] J. N Anker, W. P Hall, O. Lyandres, N. C Shah, J. Zhao, and R. P Van Duyne, Biosensing with plasmonic nanosensors, Nat. Mater. **7,** 442 (2008).

[11] A. Kinkhabwala, Z. Yu, S. Fan, Y. Avlasevich, K. Müllen, and W. E Moerner, Large single-molecule fluorescence enhancements produced by a bowtie nanoantenna, Nat. Photonics **3,** 654 (2009).

[12] J. C Ginn and I. Brener, Realizing Optical Magnetism from Dielectric Metamaterials, Phys. Rev. Lett. **108,** 097402 (2012).

[13] A. I Kuznetsov, A. E Miroshnichenko, M. L Brongersma, Y. S Kivshar, and B. Luk'yanchuk, Optically resonant dielectric nanostructures, Science **354,** 2472 (2016).

[14] J. Zhou, A. Panday, Y. Xu, X. Chen, L. Chen, C. Ji, and L. J. Guo, Visualizing Mie Resonances in Low-Index Dielectric Nanoparticles, Phys. Rev. Lett. **120,** 253902 (2018).

[15] Y. Chen, H. Liu, M. Reilly, H. Bae, and M. Yu, Enhanced acoustic sensing through wave compression and pressure amplification in anisotropic metamaterials, Nat. Commun. **5,** 5247 (2014).

[16] J. Yang, J. Chen, Y. Liu, W. Yang, Y. Su, and Z. L. Wang, Triboelectrification-based organic film nanogenerator for acoustic energy harvesting and self-powered active acoustic sensing, ACS Nano **8,** 2649 (2014).

[17] S. A. Cummer, B.-I. Popa, D. Schurig, D. R. Smith, J. Pendry, M. Rahm, and A. Starr, Scattering Theory Derivation of a 3D Acoustic Cloaking Shell, Phys. Rev. Lett. **100,** 024301 (2008).

[18] J. D. Murphy, Resonance scattering of acoustic waves from cylindrical shells, J Acoust. Soc. Am. **64,** 677 (1978).

[19] L. Zhao, B. Liu, Y. Gao, Y. Zhao, and J. Haung, Enhanced scattering of acoustic waves at interfaces, Front. Phys. **7,** 319 (2012).

[20] Y. Zhu, X. Fan, B. Liang, J. Cheng, and Y. Jing, Ultra-thin Acoustic Metasurface-Based Schroeder Diffuser, Phys. Rev. X **7,** 021034 (2017).

[21] Y. Cheng, C. Zhou, B. G. Yuan, D. J. Wu, Q. Wei, and X. J. Liu, Ultra-sparse metasurface for high reflection of low-frequency sound based on artificial Mie resonances, Nat. Mater. **14,** 1013 (2015).

[22] T. Lee and H. Iizuka, Acoustic resonance coupling for directional wave control: from angle-dependent absorption to asymmetric transmission, New J. Phys. **21,** 043030 (2019).

[23] S. Yi, M. Zhou, Z. Yu, P. Fan, N. Behdad, D. Lin, K. X. Wang, S. Fan, and M. Brongersma, Subwavelength angle-sensing photodetectors inspired by directional hearing in small animals, Nat. Nanotechnol. **13,** 1143 (2018).

[24] X. Zhu, B. Liang, W. Kan, Y. Peng, and J. Cheng, Deep-Subwavelength-Scale Directional Sensing Based on Highly Localized Dipolar Mie Resonances, Phys. Rev. Appl. **5,** 054015 (2016).

[25] W. Liu, Ultra-directional super-scattering of homogenous spherical particles with radial anisotropy, Opt. Express **23,** 14734 (2015).

[26] W. Liu, Superscattering pattern shaping for radially anisotropic nanowires, Phys. Rev. A **96,** 023854 (2017).

[27] N. N. Lebedev, *Special Functions & their Applications* (Dover Publications, New York, 1972).

[28] See the Supplemental Material at http://link.aps.org/supplemental/10.1103/PhysRevApplied.12.054059 for additional figures and notes.

[29] H. L. Chen and L. Gao, Anomalous electromagnetic scattering from radially anisotropic nanowires, Phys. Rev. A **86,** 033825 (2012).

[30] T. Lee and H. Iizuka, Bragg scattering based acoustic topological transition controlled by local resonance, Phys. Rev. B **99,** 064305 (2019).

[31] J. J. Faran, Sound scattering by solid cylinders and spheres, J. Acoust. Soc. Am. **23,** 405 (1951).

[32] C. Lagarrigue, J. P. Groby, V. Tournat, and O. Dazel, Absorption of sound by porous layers with embedded periodic arrays of resonant inclusions, J. Acoust. Soc. Am. **134,** 4670 (2013).

[33] E. Shenderov, *Wave Problems in Underwater Acoustics* (Sudostroenie, Leningrad, 1972).

[34] S. S. Rao, *Mechanical Vibrations* (Prentice Hall, Englewood Cliffs, 2011), 5th ed.

[35] R. S. Langley, Numerical evaluation of the acoustic radiation from planar structures with general baffle conditions using wavelets, J. Acoust. Soc. Am. **121,** 766 (2007).

[36] T. Mellow and L. Kärkkäinen, On the sound fields of infinitely long strips, J. Acoust. Soc. Am. **130,** 153 (2011).

[37] W. C. Chew, *Waves and Fields in Inhomogeneous Media* (IEEE, New York, 1995).

[38] N. Jiménez, V. Romero-García, V. Pagneux, and J.-P. Groby, Quasiperfect absorption by subwavelength acoustic panels in transmission using accumulation of resonances due to slow sound, Phys. Rev. B **95,** 014205 (2017).

[39] Y. Li and B. M. Assouar, Acoustic metasurface-based perfect absorber with deep subwavelength thickness, Appl. Phys. Lett. **108,** 063502 (2016).

[40] Z. Yang, J. Mei, M. Yang, N. Chan, and P. Sheng, Membrane-Type Acoustic Metamaterial with Negative

Dynamic Mass, Phys. Rev. Lett. **101**, 204301 (2008).

[41] J. Kergomard and A. Garcia, Simple discontinuities in acoustic waveguides at low frequencies: Critical analysis and formulae, J. Sound Vib. **114**, 465 (1987).

[42] L. Kinsler, A. Frey, A. Coppens, and J. Sandesr, *Fundamentals of Acoustics* (John Wiley and Sons, New York, NY, 1982), 3rd ed.

[43] Z. Zhang, Y. Tian, Y. Wang, S. Gao, Y. Cheng, X. Liu, and J. Christensen, Directional acoustic antennas based on valley-hall topological insulators, Adv. Mater. **30**, 1803229 (2018).

[44] X. Jiang, B. Liang, R. Li, X. Zou, L. Yin, and J. Cheng, Ultra-broadband absorption by acoustic metamaterials, Appl. Phys. Lett. **105**, 243505 (2014).

[45] H. Tamaru, H. Kuwata, H. T. Miyazak, and K. Miyano, Resonant light scattering from individual Ag nanoparticles and particle pairs, Appl. Phys. Lett. **80**, 1826 (2002).

[46] M. Lee, Y.-L. Kang, W.-Y. Rho, S. Kyeong, S. Jeong, C. Jeong, W.-J. Chung, H.-M. Kim, H. Kang, Y.-S. Lee, D. Jeong, and B.-H. Jun, Preparation of plasmonic magnetic nanoparticles and their light scattering properties, RSC Adv. **5**, 21050 (2015).